

# Industry-scale production of a perovskite oxide as oxygen carrier material in chemical looping

Lei Liu<sup>a</sup>, Zhenshan Li<sup>\*a</sup>, Yang Wang<sup>a</sup>, Zuoan Li<sup>b</sup>, Yngve Larring<sup>b</sup>, Ningsheng Cai<sup>a</sup>

a. Key Laboratory for Thermal Science and Power Engineering of Ministry of Education, Department of Energy and Power Engineering, Tsinghua University, Beijing 100084, China

b. SINTEF Industry, Sustainable Energy Technology, P.O. Box 124 Blindern, NO-0314 Oslo, Norway

\*Corresponding Author

Department of Energy and Power Engineering, Tsinghua University, Beijing 100084, China

Telephone number: +86-10-62789955

Fax number: +86-10-62770209

E-mail address: [lzs@mail.tsinghua.edu.cn](mailto:lzs@mail.tsinghua.edu.cn) (Z. Li)

## Abstract

How to upscale the production of oxygen carrier particles from laboratory level to industrial level is still challenging in the field of chemical looping. The upscaled oxygen carrier must maintain its physical and chemical properties. In the present contribution, a spray drying granulation protocol was developed to produce a perovskite oxygen carrier ( $\text{CaMn}_{0.5}\text{Ti}_{0.375}\text{Fe}_{0.125}\text{O}_{3-\delta}$ ) at an industrial scale. The micro-fluidized bed thermogravimetric (MFB-TGA) experiments were performed to measure the oxygen uncoupling and redox reaction kinetics under the fluidization state with enhanced heat and mass transfer, and the obtained experimental data at different temperatures were fitted by a fluidized-bed reactor coupled with a semi-empirical kinetic model. The physical and chemical properties of granulates were compared with those of the same perovskite composition

prepared at the laboratory level. The results show the volume fraction of particle size at 75-500  $\mu\text{m}$  is >90% for the upscaled granulates, and the particles show no degradation in reactivity and no agglomeration for more than 20 redox cycles at high temperatures. The heterogeneous reaction rates are high enough, especially for the oxidization, e.g. it only spent  $\sim 5$  s to achieve full oxidization. Low attrition index of 3.74 wt% was found after the five-hour attrition test. The industrial-scale particles possess similar chemical and physical properties as the laboratory-scale particles with regards to the reaction kinetics, attrition index, crystalline phase, etc. The required bed inventories and fan energy consumption were finally estimated and found to be lower than other oxygen carriers reported in the literature.

**Key words:** Large scale production; Chemical looping; Oxygen carrier material (OCM); Perovskite; Spray granulation; Kinetics; MFB-TGA

## Abbreviations

CLC	Chemical looping combustion
CLOU	Chemical Looping with Oxygen Uncoupling
CMTF_Ind	$\text{CaMn}_{0.5}\text{Ti}_{0.375}\text{Fe}_{0.125}\text{O}_{3-\delta}$ prepared at an industrial level
CMTF_Lab	$\text{CaMn}_{0.5}\text{Ti}_{0.375}\text{Fe}_{0.125}\text{O}_{3-\delta}$ prepared at a laboratory level
MFB-TGA	Micro-fluidized bed thermogravimetric analysis
OCM	Oxygen carrier material

## 1. Introduction

Chemical Looping Combustion (CLC) is considered as a cost-effective technology with inherent  $\text{CO}_2$  capture during the fossil fuel conversion for heat and power generation [1]. A general CLC system contains an air reactor and a fuel reactor. In the fuel reactor, solid fuels, coal, biomass,

Commented [ZL1]: Lei: skip this?

If you keep it, it would be sth like 'high enough to do sth, high enough for doing sth'  
Just a suggestion

petroleum coke, etc., firstly experience an endothermic devolatilization step at a high temperature, followed by an endothermic gasification step of char to produce syngas, CO and H<sub>2</sub>, and the reducing pyrolysis gas and syngas are finally converted to CO<sub>2</sub> and H<sub>2</sub>O by the solid oxygen carrier material (OCM) in the form of endothermic or exothermic gas-solid reactions. In the air reactor, the reduced OCM is oxidized and regenerated by air, generating a large amount of heat. The OCM mainly takes charge of heat and oxygen transports between the air reactor and the fuel reactor. During the solid fuel-fired CLC process, the char gasification is the rate-controlling step [1,2], which easily causes some unconverted char particles to flow into the air reactor with the OCM streams, and the carbon capture efficiency will decrease due to the char escape. To enhance the char conversion in the fuel reactor, one strategy is to employ an OCM with a capacity of releasing gaseous O<sub>2</sub> in a relatively low oxygen partial pressure (e.g. inert atmosphere) to combust the char in the fuel reactor, as referred to as the Chemical Looping with Oxygen Uncoupling (CLOU) put forward by Mattisson et al. [3,4]. Operation with the OCMs possessing CLOU property has shown higher fuel conversion or gas combustion efficiency in different-scale CLC pilots, such as 1.5 kWth [5], 10 kWth [6,7], 100 kWth [8,9], 120 kWth [10,11] and 1 MWth [12] at various spots.

Cu-based [13,14], Mn-based [15,16] and Co-based [17] metal oxides, are provided with suitable thermodynamics for oxygen uncoupling in a low oxygen partial pressure atmosphere, and are therefore proposed as the OCMs for CLOU applications. However, physical and chemical stability could be a serious issue for the above-mentioned OCMs due to phase change, agglomeration, inactivation and attrition during the redox cycles. An OCM must possess high reactivity and suitable thermodynamics, high resistance towards attrition, stable chemical and physical performances in multiple redox cycles. Perovskite oxides (formula as ABO<sub>3</sub>), such as

**Commented [ZL2]:** I am not sure if it suitable to use low oxygen partial pressure here because we do not know the meaning of low.  
Probably we can use inert directly

**Commented [ZL3]:** Skipt it?

**Commented [ZL4]:** Lei: it is very close to the mentioned metal oxides

**Commented [ZL5]:** Cycles already mean repeating

**Commented [YL6]:** Propoerties mention is general an needed both for CLC and CLOU materials

CaMnO<sub>3-δ</sub>, have shown acceptable thermodynamics for oxygen uncoupling and high reactivity for reducing gases conversion [18,19], high stability under a wide range of oxygen partial pressures and fast oxygen ionic diffusion in the bulk phase [20]. The performances of fast oxygen diffusion and exchange without phase change make some perovskite-based OCMs promising for CLOU using solid fuels. In addition, doping different metal elements on B sites could further increase reactivity and the structural stability, such as CaMn<sub>0.9</sub>Mg<sub>0.1</sub>O<sub>3-δ</sub> [19] and CaMn<sub>0.875</sub>Ti<sub>0.125</sub>O<sub>3</sub> [21] designed as OCMs for both CLOU and CLC applications. In the previous contribution, the perovskite, CaMn<sub>0.5</sub>Ti<sub>0.375</sub>Fe<sub>0.125</sub>O<sub>3-δ</sub> (CMTF), was developed for enhancing the stability via Ti addition and reactivity via Fe addition [22]. This perovskite possesses much faster oxygen uncoupling and redox kinetics than Cu- [13] and Mn-based oxygen carriers [23], and other reported perovskite oxygen carriers [19,24]. Currently, most investigations of synthetic OCMs are prepared in lab scales, with few reported large-scale fabrication [Ref, Larring]. However, the upscaling is still a big challenge to be solved when it comes to the CLC demonstration and industrial applications.

In the present work, the main objective was to address the perovskite oxygen carrier particle preparation issue at a tonne level to reach the industry-scale production of CaMn<sub>0.5</sub>Ti<sub>0.375</sub>Fe<sub>0.125</sub>O<sub>3-δ</sub> (CMTF\_Ind). Since accurate heterogeneous oxygen uncoupling and redox kinetics is crucial to determining the solid residence time and bed inventories in CLC reactor design and process optimization, we therefore measured the reaction kinetics by means of the microfluidized bed thermogravimetric analysis (MFB-TGA) based on the on-line track of mass change [23,25]. We finally evaluate the properties and performance of CMTF\_Ind (CaMn<sub>0.5</sub>Ti<sub>0.375</sub>Fe<sub>0.125</sub>O<sub>3-δ</sub> prepared at industrial level) and compare them with those of CMTF\_Lab (CaMn<sub>0.5</sub>Ti<sub>0.375</sub>Fe<sub>0.125</sub>O<sub>3-δ</sub> prepared at laboratory level).

**Commented [YL7]:** This is doped with Mg to destabilize it to give higher reactivity, with Ti it is to give higher stability.

**Commented [YL8]:** Is this under same dry H<sub>2</sub> conditions or wet H<sub>2</sub> where the pO<sub>2</sub> is higher and driving force lower. (H<sub>2</sub>O will be created in both cases and mostly dominate the driving force unless the steam content is high in the H<sub>2</sub> gas. But yes it is fast.

**Commented [YL9]:** 1. We have a paper on industrial tons scale production of CMTM in an other CLC project on NG called SUCCESS.  
2. Larring, Y., Pishahang, M., Tolchard, J., Lind, A.M., Sunding, M.F., Stensrød, R.E., Jacobs, M., Snijkers, F., van der Kolk, T., Albertsen, K. "Fabrication process parameters significantly affect the perovskite oxygen carriers materials (OCM) performance in chemical looping with oxygen uncoupling (CLOU)" *J Therm Anal Calorim.* 140 (2020) 577–589 [10.1007/s10973-018-7903-6](https://doi.org/10.1007/s10973-018-7903-6)

**Commented [YL10]:** Agree from our SUCCESS experience, but I think your result in CHEERS was much better, based on creation of a more stable and homogen perovskite. I think the way it was calcined in your case is much better than in the SUCCESS project.

## 2. Experimental

### 2.1. Oxygen carrier preparation

To produce the CMTF Ind particles, commercial  $\text{Ca(OH)}_2$  (Guanghui, China),  $\text{Mn}_3\text{O}_4$  (Zhonggang, China),  $\text{TiO}_2$  (Yuxing, China) and  $\text{Fe}_2\text{O}_3$  (Changli, China) powders were selected as the raw materials, and the compositions and purities of these raw materials measured by X-ray Fluorescence (XRF) are listed in Table 1; their size distributions are illustrated in Fig. 1. The average diameters ( $d_{50}$ ) are 3.18  $\mu\text{m}$  for  $\text{Ca(OH)}_2$ , 2.83  $\mu\text{m}$  for  $\text{Mn}_3\text{O}_4$ , 0.99  $\mu\text{m}$  for  $\text{TiO}_2$ , and 4.44  $\mu\text{m}$  for  $\text{Fe}_2\text{O}_3$ . The maximum diameter for all raw materials is within 20  $\mu\text{m}$ , fine enough for the synthesis in the next stage.

Commented [ZL11]: For industrial scale, I would like to use produce

Table 1. Compositions of the raw materials used for the CMTF\_Ind particles production

Source	Compositions (wt%)								
$\text{Mn}_3\text{O}_4$	Mn	Zn	Fe	Si	Gd	Mg	Cl	Lu	O*
	75.79	0.17	0.13	0.08	0.06	0.05	0.03	0.02	23.67
$\text{Fe}_2\text{O}_3$	Fe	Zn	Dy	Cl	Na	Mn	Se	Tm	O*
	67.81	0.97	0.26	0.22	0.14	0.13	0.12	0.14	30.21
$\text{TiO}_2$	Ti	Al	Na	Si	V	Zn	P	Zr	O*
	54.25	1.48	1.34	0.81	0.19	0.22	0.07	0.06	41.58
$\text{Ca(OH)}_2$	Ca	Mg	Sn	Pb	O*				
	51.17	1.90	0.01	0.01	46.91				

\* Oxygen calculation by difference

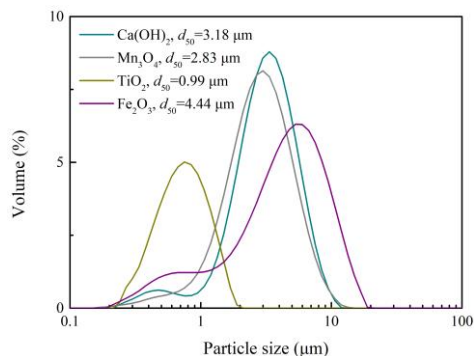


Fig.1. Size distribution of the raw materials used for the CMTF\_Ind particles production

Fines of  $\text{Ca(OH)}_2$ ,  $\text{Mn}_3\text{O}_4$ ,  $\text{TiO}_2$  and  $\text{Fe}_2\text{O}_3$  were filled in a propeller blade mixer, according to the corresponding stoichiometric ratio of the metal elements in  $\text{CaMn}_{0.5}\text{Ti}_{0.375}\text{Fe}_{0.125}\text{O}_{3-\delta}$ . Plenty of water was added into the mixer, to maintain a solid-water ratio of 2:1. After continuous stirring for two hours, binder was added to increase the suspension viscosity, followed by one-hour stirring. To eliminate the bubbles generated during the stirring process, a small fraction of the defoamer was employed. A small amount of dispersant and lubricant was then used to improve the rheology and liquidity of the suspension. The total mass fraction of the binder, defoamer, dispersant and lubricant is 1.20 wt%. The technical support of the binder, defoamer, dispersant and lubricant is from Dingsheng Spray Co., Ltd, China. Finally, the suspension was obtained for the next-step particle production.

Commented [ZL12]: Lei: the amount is the subject, same as the last sentence

CMTF\_Ind particles were fabricated by utilizing a pressure-spray drying granulation device. The maximum water evaporation of the device is  $\sim 2800$  kg/h. Prior to granulating, the spray device was heated to  $180^\circ\text{C}$ , and the gauge pressure inner the spray device was operated at  $\sim -80$  Pa via an induced draft fan. The granulation process is demonstrated in Fig. 2. The prepared suspension, from the mixer, was pressed to 3.5 MPa and was pumped to single-fluid high-pressure nozzles located at the top of the spray device. The suspension was sprayed downward and was atomized into droplets

through the single-fluid high-pressure nozzles, following the droplets moved down due to the gravity and hot air. In the process of droplets falling, the water was quickly evaporated, which causing spherical particles formation due to surface tension. Finally, the dry particles were continuously collected at the bottom of the spray drying device. The particles were continuously manufactured at a production scale of ~2500 kg/h, and ~1000 kg particles were synthesized within half an hour at present.

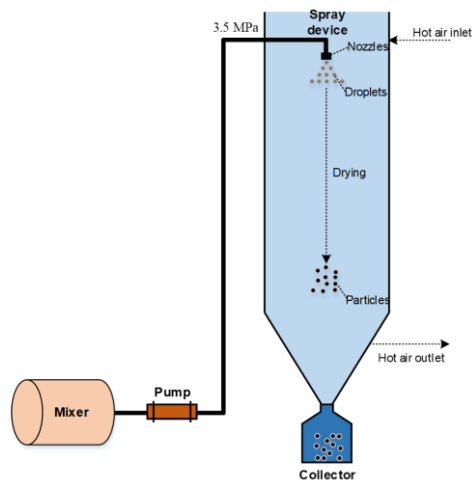


Fig. 2. Process flow diagram for the spray drying granulation

The parameters, nozzle pressure, nozzle size, suspension rheology, drying temperature, etc., were adjusted, to obtain a reasonable particle size range. It can be seen from Fig. 3 that the volume fraction of the particle size at 75-500  $\mu\text{m}$  is ~90%, and the average diameter ( $d_{50}$ ) of the prepared CMTF\_Ind particles is 195  $\mu\text{m}$ .

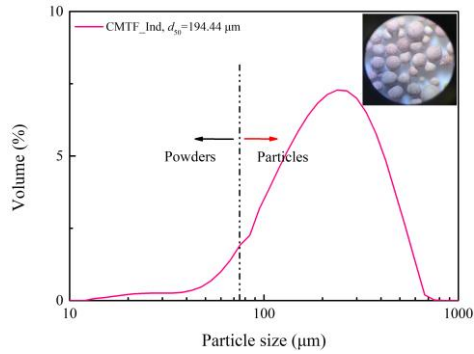


Fig. 3. Size distribution of the CMTF\_Ind particles

Finally, calcination was performed in air at 1350 °C for 8 hours, to obtain CMTF\_Ind particles with the desired crystalline phases and with sufficient mechanical strength. The total cost for the CMTF\_Ind particle production is ~2000 US\$/ton-OCM, containing the raw materials, spray drying granulation, and calcination. The detailed cost estimation can be found in the [supporting information](#).

After calcination, CMTF\_Ind was characterized X-ray Fluorescence (XRF), and its compositions were compared with CMTF\_Lab, see [Table 2](#). It can be seen that the oxide constitutions of CMTF\_Ind are very close to that of CMTF\_Lab,. For example, the mass fractions of MnO are 29.06 wt% for CMTF\_Lab and 30.29 wt% for CMTF\_Ind.

Table 2. Comparison of compositions between CMTF\_Lab and CMTF\_Ind

Composition (wt%)	CaO	MnO	TiO <sub>2</sub>	Fe <sub>2</sub> O <sub>3</sub>
CMTF_Lab	40.82	29.06	19.16	8.27
CMTF_Ind	39.04	30.29	19.54	8.07

## 2.2. Micro-fluidized bed thermogravimetric analysis (MFB-TGA)

The isothermal kinetic experiments of the manufactured CMTF\_Ind particles, including oxygen uncoupling, oxidization and reduction reactions, were performed by using a micro-fluidized



bed thermogravimetric analysis technology (MFB-TGA) [23,25,26]. As shown in Fig. 4(a), the MFB-TGA mainly contains a furnace, a fluidized-bed reactor with an inner diameter of 30 mm, a gas supply system, and a measuring system, of which the fluidized-bed reactor is the core of the MFB-TGA. The reactor is made of quartz, and a porous quartz plate is used as the gas distributor. The bed temperature above the gas distributor was recorded by a K-type thermocouple, and the pressure drop of the fluidized-bed reactor was measured by a differential pressure sensor.

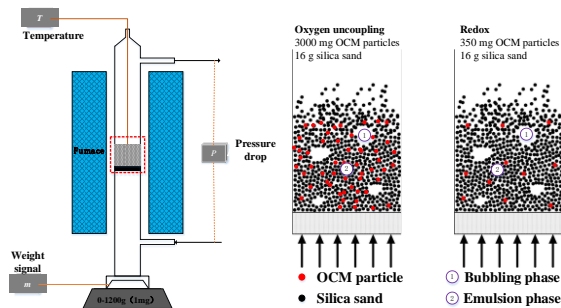


Fig. 1. Schematic diagrams of (a) the MFB-TGA apparatus and (b) the solid particles in the bubbling bed reactor

The flow rates of fluidizing agents were controlled by well-calibrated mass flowmeters. The gas flowed into the bottom of the micro-fluidized bed reactor through switching well-connected magnetic valves. A mass transducer with a measurement accuracy of 1 mg was applied to measure the whole weight including the reactor and bed materials. The measurement error of the MFB-TGA is within  $\pm 1$  mg, which guarantees that the mass change is mainly caused by the gas-solid reaction between samples and gas phases [22]. More details about this technique can be found elsewhere [23,25,26].

For the oxygen uncoupling kinetic tests,  $\sim 16$  g silica sand (300-350  $\mu\text{m}$ ) was filled in the reactor as the bed material; the reactor with a 21 vol%  $\text{O}_2$  fluidizing gas of 1.2 L/min (STP) was

Commented [YL13]: Repeated below

Commented [YL14]: See comment below, where you repeat this part

Commented [III5R14]: Thanks, Yngve. I feel keep the description about the error here is better

Commented [YL16R14]: ok

heated to 800-930 °C; ~ 3000 mg fully oxidized CMTF\_Ind particles (180-250 μm) were added into the reactor; once mass and temperature signals were stable, to eliminate the initial effect produced by calcination stage 6 redox cycles were performed by switching the fluidizing agents between 10 vol% H<sub>2</sub> and 21 vol% O<sub>2</sub>, before least 3 isothermal O<sub>2</sub> release and uptake cycles were carried out to measure the oxygen uncoupling kinetics by switching the fluidizing gases between 100 vol% N<sub>2</sub> and 21 vol% O<sub>2</sub>. For the oxidization and reduction kinetic tests, ~ 16 g silica sand (300-350 μm) was filled as the bed material, before ~ 350 mg CMTF\_Ind particles (180-250 μm) was added, the reactor was heated to 750-900 °C, and a 21 vol% O<sub>2</sub> was introduced to act as the fluidizing gas; isothermal redox cycles were performed by switching the fluidizing gases between 21 vol% O<sub>2</sub> and 10 vol% H<sub>2</sub>, or 21 vol% O<sub>2</sub> and 10 vol% CH<sub>4</sub>; to prevent direct mixing of the reducing and oxidizing gases, 100 vol% N<sub>2</sub> was introduced for 30 s between the reduction stage and oxidization stage. The gas flowrates of the fluidizing agents were controlled at 1.2-1.5 L/min (STP), corresponding to a superficial velocity of 3-5  $U_{mf}$ . The reactor was hence operated at the bubbling state. **The gas switch was realized through the well-connected magnetic valves.** Therefore, the mass change is only arisen from the gas-solid reactions between solid CMTF\_Ind particles and gas phases. The active lattice oxygen in CMTF\_Ind would be lost during the oxygen release and reduction, causing the particle mass to decrease, while the reduced CMTF\_Ind obtained the lattice oxygen again during the oxidization, causing the particle mass to increase. The principle of the MFB-TGA is to monitor the mass change in real-time, to obtain the reaction kinetics close to the real fluidization condition with enhanced heat and mass transfer.

### 2.3. Particle characterization and Data **evaluation**

X-ray Diffraction (XRD, Rigaku D/max-2550@3-70°) analysis was conducted to determine

**Commented [YL17]:** could maybe be better with collection (you do not evaluate the data in 2.3) If you use evaluation you should say a little more concrete about how you will interpret/evaluate the data. Or add: This model will be used for interpretation and evaluation of the data. Model for data evaluation is in 3.1 correct?

**Commented [ZL18R17]:** Probably this part can follow the MFB-TGA directly rather than single it out directly. You can follow that part by the measured mass is used to calculate conversion of redox through. You can shorten it.

the crystal phases of the fresh CMTF\_Lab, fresh CMTF\_Ind, and tested CMTF\_Ind. The mercury intrusion method (AutoPore IV 9500, Micromeritics) was applied to measure the porosity, and the nitrogen adsorption experiments (Micromeritics ASAP 2460) were performed at 77 K to obtain the BET surface area and BJH pore diameter. The morphology of the CMTF\_Ind particle and cross-section was characterized by a scanning electron microscope (Zeiss Merlin, [0.8nm@15kV](#)).

The online mass signals,  $m(t)$ , are collected by the mass transducer during the oxygen uncoupling and redox experiments. The conversion level of the oxygen uncoupling reactions can be described as Eq. (1), and the conversion levels for the reduction ( $X_r$ ) and oxidization ( $X_o$ ) reactions were described as Eqs. (2) and (3). The numerator in Eqs. (1)-(3) refers to the mass change caused by the heterogeneous gas-solid reactions.

$$X_{ou}(t) = \frac{m_o - m(t)}{R_{oc,ou} m_{oc}} \quad (1)$$

$$X_r(t) = \frac{m_o - m(t)}{R_{o,t} m_{oc}} \quad (2)$$

$$X_o(t) = \frac{m(t) - m_r}{R_{o,t} m_{oc}} \quad (3)$$

where  $m_o$  is the total mass of the reactor and bed materials (silica sand and fully oxidized CMTF\_Ind particles),  $m_r$  is the total mass of the reactor and bed materials (silica sand and fully reduced CMTF\_Ind particles),  $m_{oc}$  is the mass of CMTF\_Ind particles added into the reactor. The oxygen transfer capacity for oxygen uncoupling ( $R_{oc,ou}$ ) is 0.88 wt% for 850 °C, 0.82 wt% for 900 °C, and 0.70 wt% for 930 °C, according to the theoretical calculation [22], while the total oxygen transfer capacity ( $R_{o,t}$ ) was determined by the experiments.

**Commented [ZL19]:** Lei: maybe you can take out this part as a separate? It is bizarre to put powder characterization and data evaluation

### 3. Models

#### 3.1. Model for oxygen uncoupling reaction

The CMTF\_Ind particles release gaseous O<sub>2</sub> in the bubbling-bed reactor at the pure N<sub>2</sub> condition during the oxygen uncoupling reaction. It is well known that the bed zone in the reaction can be divided into two phases, of which the bubble phase stores the majority of fluidizing gases, and the emulsion phase contains almost all particles. Therefore, the CMTF\_Ind particles mainly release gaseous O<sub>2</sub> in the emulsion phase, and the driving force is  $(C_{eq,O_2} - C_{e,O_2})$ . The released O<sub>2</sub> will firstly diffuse to the emulsion phase through the external mass transfer around the particle, then to the bubble phase due to the concentration gradient. An O<sub>2</sub> concentration profile along the axial direction will be produced in the emulsion phase and the bubble phase. The released O<sub>2</sub> finally leaves the reactor. A reactor model should be used to describe the O<sub>2</sub> transfer process in the reactor.

Commented [YL20]: Should be or is used?

The simplified two-phase model, derived from the classic Kunii and Levenspiel model (K-L model) [27], could relate the reaction and the gas diffusion between the bubble phase and the emulsion phase [22,23], see Eq. (4). The simplified K-L model is based on the mass balance with the assumptions that there are no solids in the bubble phase. The first equation in Eq. (4) describes the O<sub>2</sub> concentration profile in the emulsion phase, affected by the oxygen uncoupling reaction and interphase gas exchange. The second equation in Eq. (4) describes the O<sub>2</sub> concentration profile in the bubble phase, only affected by the O<sub>2</sub> transfer from the emulsion phase.

$$\begin{cases} -(1-\theta)U_{mf} \frac{dC_{e,O_2}}{dz} = -f_a(1-\theta)(1-\varepsilon_{mf})K_r(C_{eq,O_2} - C_{e,O_2}) + \theta K_{bc}(C_{e,O_2} - C_{b,O_2}) \\ -U_b^* \frac{dC_{b,O_2}}{dz} = -K_{bc}(C_{e,O_2} - C_{b,O_2}) \end{cases} \quad (4)$$

where  $C_{b,O_2}$  (mol/m<sup>3</sup>) and  $C_{e,O_2}$  (mol/m<sup>3</sup>) stand for the O<sub>2</sub> concentrations in the bubble phase and

the emulsion phase respectively,  $C_{eq,O_2}$  (mol/m<sup>3</sup>) refers to the equilibrium O<sub>2</sub> concentration.  $U_b^*$  (m/s) and  $U_{mf}$  (m/s), are the effective gas velocity in the bubble phase and the minimum fluidization gas velocity. The parameters,  $f_a$  and  $\theta$ , are the volume fraction of the CMTF\_Ind particles in all solid volume and the bubble fraction. All the coefficients can be calculated, see the [supporting information](#). The only undefined parameter is the reaction rate constant ( $K_r$ , s<sup>-1</sup>), which can be expressed as

$$\begin{cases} K_r = \frac{1}{\frac{1}{K_i} + \frac{d_p}{6k_g}} \\ K_i = \frac{R_{OC,oi}\rho_s}{2M_O} \{k_{chem}(\psi X_e - X_{chem})^{2/3} + k_{diff}[(1-\psi)X_e - X_{diff}]^{2/3}\} \\ k_g = (Sh \cdot D_{O_2})/d_p \end{cases} \quad (5)$$

where  $k_g$  (m/s) refers to the external mass transfer coefficient, and  $Sh$  is the Sherwood number.  $K_i$  (s<sup>-1</sup>) refers to the comprehensive reaction rate constant of the particle, which can be obtained with the given rate constants ( $k_{chem}$  and  $k_{diff}$ ) and the ratio of the conversion level at the first reaction stage to the total conversion level ( $\psi$ ). The value of  $K_r$  is then calculated from [Eq. \(5\)](#). A semi-empirical model [\[22\]](#) with two equations was employed to describe the conversion vs. time, see [Eq. \(6\)](#). The kinetic model includes two independent equations, where the former and the latter are used to fit the experimental data in the first reaction stage and the second reaction stage respectively. The total conversion ( $X$ ) is the sum of the first stage conversion ( $X_{chem}$ ) and the second stage ( $X_{diff}$ ).

$$\begin{cases} \frac{dX_{chem}}{dt} = k_{chem}(\psi X_e - X_{chem})^{2/3} (C_{eq,O_2} - C_{e,O_2}) \\ \frac{dX_{diff}}{dt} = k_{diff}[(1-\psi)X_e - X_{diff}]^{2/3} (C_{eq,O_2} - C_{e,O_2}) \\ X = X_{chem} + X_{diff} \end{cases} \quad (6)$$

The rate constants ( $k_{chem}$  and  $k_{diff}$ ) and the ratio ( $\psi$ ) can be written as Arrhenius expressions,

$$k_{\text{chem}} = A_{0,\text{chem}} \exp\left(-\frac{E_{\text{chem}}}{RT}\right) \quad (7)$$

$$k_{\text{diff}} = A_{0,\text{diff}} \exp\left(-\frac{E_{\text{diff}}}{RT}\right) \quad (8)$$

$$\psi = A_{0,L} \exp\left(-\frac{E_L}{RT}\right) \quad (9)$$

### 3.2. Model for oxidation and reduction reactions

Different from the oxygen uncoupling, the mass transfer direction is opposite for the oxidization and reduction reactions. The reaction gases initially exist in the bubble phase, then diffuse to the emulsion phase through the interphase gas exchange, further transfer to the oxygen carrier particle surface through the external mass transfer. The chemical reactions finally occur. To analyze the experimental data from the MFB-TGA, the simplified K-L model was also used to describe the chemical reaction and the mass transfer between the phases:

$$\begin{cases} -U_b \frac{dC_{b,i}}{dz} = K_{be}(C_{b,i} - C_{e,i}), (i = \text{O}_2, \text{H}_2, \text{CH}_4) \\ -(1-\theta)U_{mf} \frac{dC_{e,i}}{dz} = -\theta K_{be}(C_{b,i} - C_{e,i}) + f_a(1-\theta)(1-\varepsilon_{mf})K_r(C_{e,i} - C_{eq,i}), (i = \text{O}_2, \text{H}_2, \text{CH}_4) \end{cases} \quad (10)$$

How to calculate the parameters in Eq. (10) has been introduced in Section 3.1.  $K_r$  ( $\text{s}^{-1}$ ) couples the reaction term and the external mass transfer term, as

$$\begin{cases} K_r = \frac{1}{\frac{1}{K_n} + \frac{d_p}{6k_g}} \\ K_n = \frac{R_{0,M} \rho_s}{\alpha M_O} \{k_{\text{chem}}(\psi X_e - X_{\text{chem}})^{2/3} + k_{\text{diff}}[(1-\psi)X_e - X_{\text{diff}}]^{2/3}\} \\ k_g = (Sh \cdot D_i)/d_p, (i = \text{O}_2, \text{H}_2, \text{CH}_4) \end{cases} \quad (11)$$

The above semi-empirical model including the two stages was also used to fit the conversion curves of the oxidation and reduction reactions, see Eq. (12). The rate constants ( $k_{\text{chem}}$  and  $k_{\text{diff}}$ ) and the ratio ( $\psi$ ) can be written as Arrhenius expressions.

$$\left\{ \begin{array}{l} \frac{dX_{\text{chem}}}{dt} = k_{\text{chem}} (\psi X_e - X_{\text{chem}})^{2/3} (C_{e,i} - C_{e,q,i}), \quad (i = \text{O}_2, \text{H}_2, \text{CH}_4) \\ \frac{dX_{\text{diff}}}{dt} = k_{\text{diff}} [(1 - \psi) X_e - X_{\text{diff}}]^{2/3} (C_{e,i} - C_{e,q,i}), \quad (i = \text{O}_2, \text{H}_2, \text{CH}_4) \\ X = X_{\text{chem}} + X_{\text{diff}} \end{array} \right. \quad (12)$$

## 4. Results and discussions

### 4.1. Multiple redox cycles and typical test

The redox multicycles at 900 °C of the prepared CMTF\_Ind are shown in Fig. 2. The reduction and oxidization reactions were performed in 10 vol% H<sub>2</sub> and 21 vol% O<sub>2</sub>. The first cycle was carried out with the longest reduction time (300 s) and oxidization time (120 s), to measure the total oxygen transfer capacity ( $R_{\text{OC},i}$ ) of CMTF\_Ind. It can be seen that the mass continuously decreased during the reduction, since the active oxygen in CMTF\_Ind was taken away in the form of H<sub>2</sub>O. The final mass loss is 5.71 wt%, and the lost mass was fully gained during the following oxidization, implying that the total oxygen transfer capacity ( $R_{\text{OC},i}$ ) is 5.71 wt%. For the 2<sup>nd</sup> – 4<sup>th</sup> cycles, the reduction time was stayed at 300 s, whereas the oxidization time was halved (60 s). The mass change is still 5.71 wt% during the redox cycles, and the reduced CMTF\_Ind can be fully regenerated after oxidization. Furthermore, the oxidization time was unchanged, while the reduction time was decreased to 180 s. The mass change was stabilized at 5.71 wt% as well. The redox period was finally shortened to 90 s for reduction and 30 s for oxidization, to complete the whole multiple cycles test. It can be observed that neither the oxygen transfer capacity nor the chemical performance has been influenced. The shortest redox period indicates CMTF\_Ind possesses fast lattice oxygen exchange ability with the reacting gases. The measured oxygen transfer capacity (5.71 wt%) is exactly equal to that of CMTF\_lab [22]. A combination of the pressure drop curves (Fig. 2) and the real-time fluidization video (supporting video) demonstrates that agglomeration did not occur during the redox, showing

that the synthesized CMTF\_Ind particles possess acceptable fluidization property.

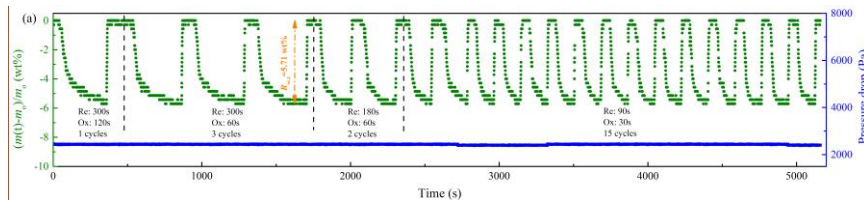


Fig. 2. Mass variation during the multiple redox cycles in the MFB-TGA at 900 °C (oxidization by 21 vol% O<sub>2</sub> and reduction by 10 vol% H<sub>2</sub>)

A typical redox cycle is shown in Fig. 3. The weight of OCM was decreasing after altering the fluidizing gas to 10 vol% H<sub>2</sub>. Once full oxygen capacity of CMTF\_Ind was consumed, the OCM was fully reduced, and the weight of OCM was unchanged. The weight loss is 20 mg, corresponding to a total oxygen transfer capacity of 5.71 wt%. The oxidation step fully regenerated the lattice oxygen.

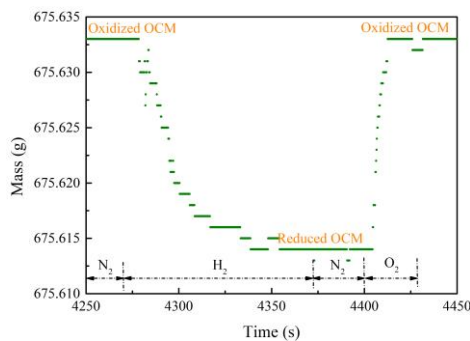


Fig. 3. A typical redox cycle in the MFB-TGA at 900 °C (oxidization by 21 vol% O<sub>2</sub> and reduction by 10 vol% H<sub>2</sub>)

#### 4.2. Comparison of heterogeneous reaction kinetics

The measured heterogeneous reaction rates of CMTF\_Ind were compared with CMTF\_lab at 900 °C, see Fig. 4. The whole process of the oxygen uncoupling reaction of CMTF\_Ind includes

**Commented [ZL21]:** With 300s reduction, I think the mass change is still decreasing, while 180 and 90s give same values.

**Commented [YL22R21]:** Yes on the first cycle on the fourth it is stable. Most likely a small activation of the material. But the capacity measured is constant.

**Commented [H23R21]:** In fact, in the experments, I found the second reaction stage of CMTF\_Ind is quite slower than that of CMTF\_Lab for the former 10 cycles, but it recovered after 10 cycles. It means the reaction rate of the second stage was increasing. So from 1-3 cycles, the activation might not occur. Just because the reduction time was not long enough.

**Commented [ZL24R21]:** It is interesting to see the industrialized sample needs to be activated somehow considering homogeneous compositions from XRF

**Commented [ZL25]:** Is it humidified or dry?

**Commented [H26R25]:** Dry H2

**Commented [ZL27R25]:** Ok, so that the driving force is high.



two stages: one is the first fast O<sub>2</sub> release stage, and the other is the second slow O<sub>2</sub> release stage. It will take ~20 s to reach the critical conversion level of 0.35, as seen in Fig. 4(a). There are similar oxygen uncoupling rates between CMTF\_Ind and CMTF\_Lab. The oxidization will be fully completed within ~5 s, whether it is CMTF\_Ind or CMTF\_Lab (Fig. 4(b)), indicating an ultrafast oxidization rate. When CMTF\_Ind is reduced by 10 vol% H<sub>2</sub>, the reaction consists of a fast reduction stage and a slow reduction stage, and the reduction rate decreases with the conversion at the slow stage, as shown in Fig. 4(c). The full reduction will be finished within ~30 s. The reduction rate of CMTF\_Ind is very close to that of CMTF\_Lab. The reaction rate with CH<sub>4</sub> is apparently ~8 times slower than that with H<sub>2</sub>, see Fig. 4(d). The reduction can also be divided into an initial fast stage followed by a slow stage, and the required time for reaching the critical conversion is ~100 s. From the above comparisons, the heterogeneous reaction rates of CMTF\_Ind are similar to those of CMTF\_Lab, implying the upscaling granulation is successful from the view of chemical performance.

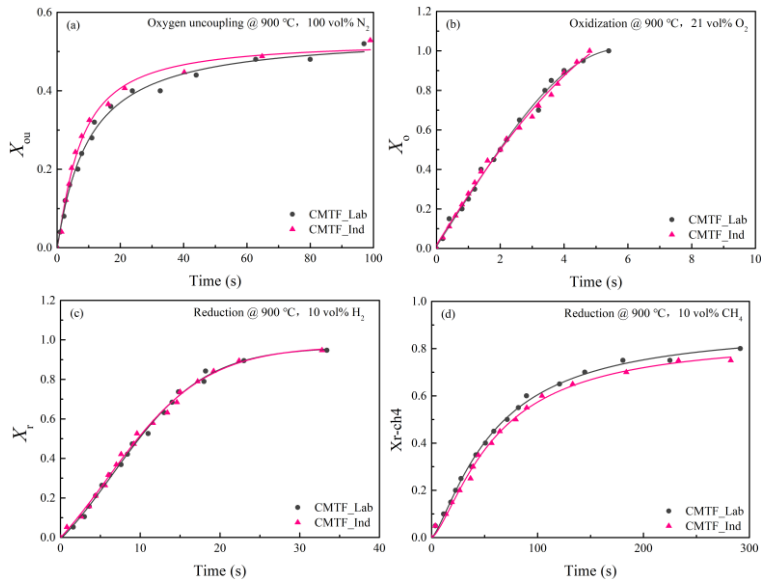


Fig. 4. Comparison of the heterogeneous reaction kinetics between CMTF\_Ind and CMTF\_Lab. (a) oxygen uncoupling reaction; (b) oxidation reaction; (c) reduction reaction with H<sub>2</sub>; (c) reduction reaction with CH<sub>4</sub>

### 4.3. Kinetics determination for heterogeneous reaction

Reaction kinetic parameters are significantly important to determine the solid bed inventory and solid residence time in the air reactor and the fuel reactor. In this work, the oxygen uncoupling and redox kinetics were measured by using the MFB-TGA technology.

#### 4.3.1. Oxygen uncoupling reactions

The oxygen uncoupling kinetics was measured in the temperature range of 850-930 °C, see Fig. 5. The oxygen uncoupling rate increases with the rising temperature. For any temperature, the kinetic curve contains an initial fast O<sub>2</sub> release stage followed by a slower stage. The critical conversion decreases from 0.4 to 0.3 when the reaction temperature decreases from 930 °C to 850 °C.

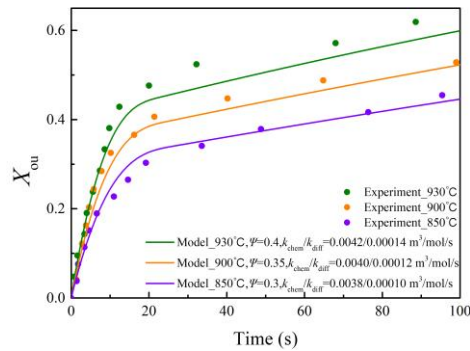


Fig. 5. Experimental and model results of oxygen uncoupling reaction at 850-930 °C

Now that the oxygen uncoupling rates are similar between CMTF\_Ind and CMTF\_Lab, we used the same kinetic parameters (pre-exponential factors and activation energies) as CMTF\_Lab, see Table 3 [22]. The rate constants ( $k_{chem}$  and  $k_{diff}$ ) and the ratio ( $\Psi$ ) at different temperatures can

be further calculated according to Eqs. (7)-(9). Introduced the calculated rate constants ( $k_{\text{chem}}$  and  $k_{\text{diff}}$ ) and the ratio ( $\Psi$ ) into the reactor model coupled with the kinetic model, the kinetic curves predicted by the model can be obtained, and the model results are illustrated in Fig. 5. It can be seen that the model could fit the experimental data well.

Table 3. Kinetic parameters for the oxygen uncoupling reaction [22]

Parameter	$E_L$	$E_{\text{chem}}$	$E_{\text{diff}}$	$A_{0,L}$	$A_{0,\text{chem}}$	$A_{0,\text{diff}}$
Unit	kJ/mol	kJ/mol	kJ/mol	n.a.	$\text{m}^3/\text{mol}/\text{s}$	$\text{m}^3/\text{mol}/\text{s}$
Value	37.86	12.36	45.12	17.33	$1.43 \times 10^{-2}$	$1.25 \times 10^{-2}$

#### 4.3.2. Oxidization and reduction reactions

The oxidization kinetics in the temperature range of 750-900 °C were measured, see Fig. 6. Like CMTF\_Lab [22], the oxidization rate is ultrafast and the required time to achieve complete oxidization is ~5 s. The oxidization only consists of a fast reaction stage. The oxidization is insensitive to the reaction temperatures, like CMTF\_Lab [22] and some other oxygen carriers [19,24].

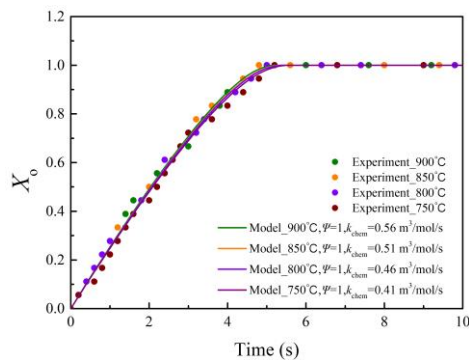


Fig. 6. Experimental and model results of oxidization reaction at 750-900 °C

The measured reduction reaction kinetics with 10 vol% H<sub>2</sub> and 10 vol% CH<sub>4</sub> are shown in Fig.

**Commented [ZL28]:** Lei: can you comment a few words here? For example, the diffusion is too fast in the bulk phase as compared to surface exchange (chemical reaction here)?

7. The conversion vs time curves of reduction by H<sub>2</sub> and CH<sub>4</sub> are composed of an initial fast reduction stage and a second slow reduction stage. The reduction rates with H<sub>2</sub> and CH<sub>4</sub> could be enhanced with the increasing temperature. The difference is the reduction rates with H<sub>2</sub> are significantly faster than the reduction rates with CH<sub>4</sub>, and the temperature effect is stronger for the reduction by CH<sub>4</sub>. The needed time for full reduction with H<sub>2</sub> is ~30 s at 900 °C, and the reduction with CH<sub>4</sub> is ~8 times longer than that with H<sub>2</sub> at 900 °C.

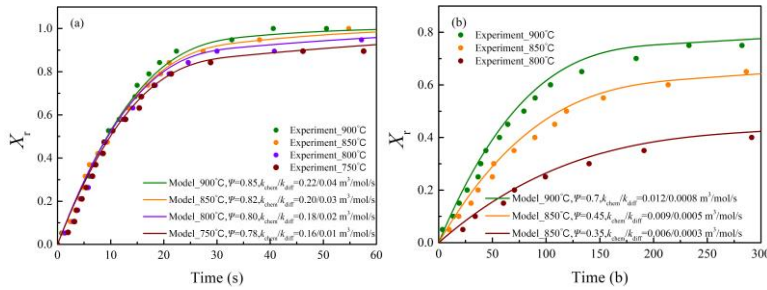


Fig. 7. Experimental and model results of reduction reactions with (a) H<sub>2</sub> and (b) CH<sub>4</sub>

According to section 4.2, there are similar oxidization and reduction rates between CMTF\_Lab and CMTF\_Ind, so are the pre-exponential factors and activation energies of the rate constants ( $k_{chem}$  and  $k_{diff}$ ) and the ratio ( $\Psi$ ), see Table 4 [22]. Employing the kinetic parameters in the below table, the rate constants ( $k_{chem}$  and  $k_{diff}$ ) and the ratio ( $\Psi$ ) can be obtained according to the Arrhenius equations (Eqs. (7)-(9)). Inputting the values of  $k_{chem}$ ,  $k_{diff}$  and  $\Psi$  into the simplified two-phase model coupled with the two-stage kinetic model, the model predicted results can be obtained, see Fig. 6 and Fig. 7. The model could reproduce the experimental data and describe the two-stage behavior well. The accurate kinetics should be obtained under enough reacting gases, to avoid diffusion control. The analysis of mass transfer resistance has been done for the redox of CMTF\_Lab [22]. Since the used model and experimental conditions are the same as the previous work [22], the effect of interphase gas diffusion and external gas diffusion can be found in the kinetics determination of

CMTF\_Lab [22]. All in all, the mass transfer rate is high enough for the chemical reactions, therefore the measured kinetic parameters in MFB-TGA are reliable.

Table 4. Kinetic parameters for the oxidization and reduction reactions [22]

Parameter	$E_L$	$E_{chem}$	$E_{diff}$	$A_{0,chem}$	$A_{0,chem}$	$A_{0,diff}$
Unit	kJ/mol	kJ/mol	kJ/mol	n.a.	m <sup>3</sup> /mol/s	m <sup>3</sup> /mol/s
O <sub>2</sub>	n.a.	18.77	n.a.	n.a.	3.80	n.a.
H <sub>2</sub>	5.86	27.62	78.13	1.55	3.86	1.01×10 <sup>2</sup>
CH <sub>4</sub>	72.19	72.67	102.63	1.10×10 <sup>2</sup>	20.98	29.74

#### 4.4. Particle characterization

##### 4.4.1. Attrition test and particle analysis

The particle attrition tests of CMTF\_Lab and CMTF\_Ind were performed and compared. The attrition resistance was measured by applying an air jet attrition apparatus, and the test method strictly followed procedures in the ASTM D5757 standard [28]. The size of the air jet attrition apparatus and more details about the attrition test can be found elsewhere [29,30]. The particle size used for the test is 120-200 μm, and 50 g particles were filled in the air jet attrition apparatus, where the fines were produced from the frequent collision among the particles. By weighing the amount of fines collected, the attrition index results can be obtained, and plotted in Fig. 8. The five-hour attrition tests show the attrition index of CMTF\_Lab and CMTF\_Ind are almost the same (3.70 wt% for CMTF\_Lab and 3.74 wt% for CMTF\_Ind). According to Cabello et al. [29], when the value of the attrition test is < 5%, the particle lifetimes usually can reach > 2000 h. For comparison, the CaMn<sub>0.9</sub>Mg<sub>0.1</sub>O<sub>3.5</sub> oxygen carrier has an attrition index of 14.1 wt% [29], and its lifetime was

evaluated to be 12000 h in a 10 kW<sub>th</sub> CLC unit [6]. Therefore, the CMTF\_Ind particle is expected to possess an even longer lifetime.

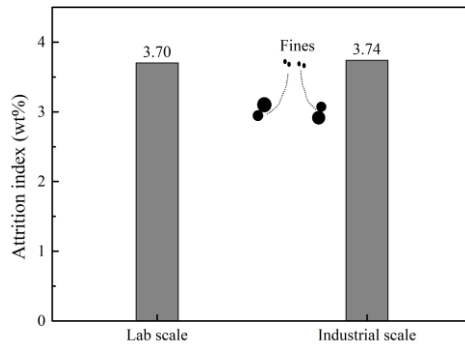


Fig. 8. Attrition test results of CMTF\_Lab and CMTF\_Ind

Other physical properties, such as BET surface area, particle pore diameter, porosity, etc., are listed in Table 5. According to the nitrogen intrusion results, the BET surface area and BJH pore diameter of the fresh CMTF\_Ind are 0.15 m<sup>2</sup>/g and 2.11 nm, which is lower than that of the fresh CMTF\_Lab. The mercury intrusion results show that the fresh CMTF\_Ind has a particle porosity of 0.45, which is slightly high than the fresh CMTF\_Lab porosity of 0.48. According to the helium intrusion results, the true densities of the fresh CMTF\_Ind and CMTF\_Lab are 4227 kg/m<sup>3</sup> and 4488 kg/m<sup>3</sup>, respectively. After multi redox cycles, all the above mentioned physical parameters of CMTF\_Ind increase except for true density. For example, the BET surface area and porosity of the tested CMTF\_Ind increase slightly to 0.31 m<sup>2</sup>/g and 0.50, respectively.

Table 5. Physical properties of the fresh CMTF\_Lab, fresh CMTF\_Ind and tested CMTF\_Ind

	BET (m <sup>2</sup> /g)	BJH pore diameter(nm)	Porosity	True density (kg/m <sup>3</sup> )
Fresh CMTF_Lab	0.21	7.56	0.48	4488
Fresh CMTF_Ind	0.15	2.11	0.45	4227

Commented [ZL29]: Lei: pls specify the time for such a mass loss if you do not use it in y-axis

Commented [H30R29]: It is 3.74wt% fines was attrited in the 5 hour test, means the attrition index is 3.74 wt%, rather than the attrition rate (3.74/5 wt%)

Commented [ZL31R29]: OK

Commented [ZL32]: Lei: what do you want to mean here for such increased properties? Does this mean that such a degradation is acceptable?

Commented [YL33R32]: True density is constant, but surface area increased from 0.15 to 0.31 is not detrimental, often a factor of 10 and above is seen if you get swelling/recrystallisation. This number will only give a slightly higher activity which is good.

Commented [H34R32]: Thanks for the comments!

Commented [ZL35R32]: I think the reactivity is almost constant from redox cycles.

Tested CMTF_Ind	0.31	7.25	0.50	4115
-----------------	------	------	------	------

#### 4.4.2. Crystalline phase analysis

The XRD patterns of the prepared CMTF\_Ind and CMTF\_Lab show a pure phase has been obtained. After a long-term redox test, the position of XRD peaks of the tested CMTF\_Ind is unchanged, indicating the crystalline phases kept unchanged. No phase separation or phase change occurs, indicating very good chemical stability of upscaled CMTF\_Ind under harsh redox cycles.

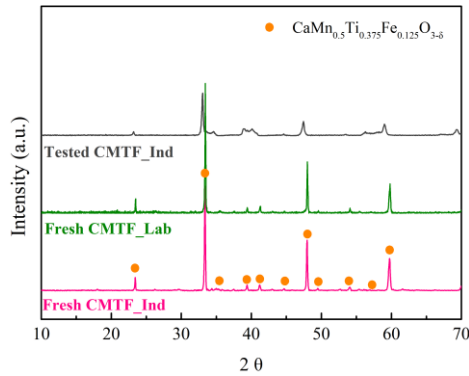


Fig. 9. Crystalline phase analysis of the fresh CMTF\_Lab, fresh CMTF\_Ind and tested CMTF\_Ind

#### 4.4.3. Particle morphology

The morphology of particle surface and cross-section of the fresh CMTF\_Ind and the tested CMTF\_Ind is demonstrated in Fig. 10. The fresh CMTF\_Ind particle is almost spherical, and the particle is quite integral. The particle contains plenty of grains, and the grain boundaries on the particle surface are significantly clear. The integration of the fresh CMTF\_Ind particle is also shown in the morphology of the cross-section inside the particle. There are some macro-pores existing inside the particle, but the solid structure is very dense around the macro-pores. For the tested CMTF\_Ind particle, apparent cracks are formed on the particle. During the multiple redox test, the

CMTF\_Ind particle continuously collided with other CMTF\_Ind particles and silica sand particles, which may be the cause of the crack formation. The obvious grain boundaries can also be found on the particle surface, the distinction is the grain surface becomes more rough, resulting in an increase in the specific surface area as listed in Table 5. Apart from the macro-pores inside the particle, amounts of micro-pore formed after the test. The newly formed porosity could promote gas diffusion inside the particle.

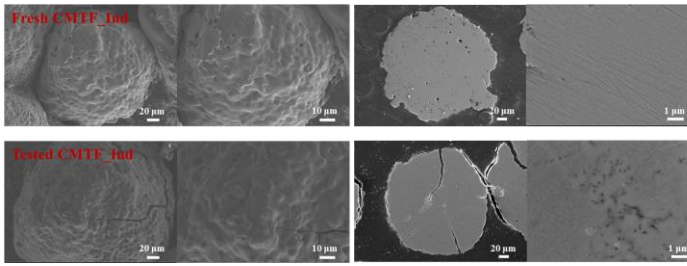


Fig. 10. Particle surface and cross-sectional SEM morphology of the fresh and tested

CMTF\_Ind

## 5. Applications to a CLC unit

The obtained kinetic parameters were then applied to acquire the design and operation criteria for CLC reactors, such as the solid bed inventory in each reactor, and energy consumption of fan to overcome the bed pressure, etc. According to the oxygen mass balance, the minimum solid inventories can be calculated as Equation (13) for the air reactor and Equation (14) for the fuel reactor [31].

$$m_{OC,AR} = \frac{10^3 m_O}{H_{fuel} R_{OC,t}} \frac{1}{[dX_o/dt]_{\bar{x}_{O_2,AR}}} \quad (13)$$

$$m_{OC,FR} = \frac{10^3 m_O}{H_{fuel} R_{OC,t}} \frac{1}{[dX_f/dt]_{\bar{x}_{H_2,FR}}} \quad (14)$$

where  $m_O$  (kg-O<sub>2</sub>/kg-fuel) is the oxygen mass required for full combustion per kg of solid fuel,



$H_{\text{fuel}}$  (kJ/mol) is the low heat value (LHV) of the solid fuel.  $m_{\text{OC,AR}}$  (kg/MW<sub>th</sub>) and  $m_{\text{OC,FR}}$  (kg/MW<sub>th</sub>) are the minimum solid inventories in the air reactor and the fuel reactor, respectively.  $\bar{x}_{\text{O}_2,\text{AR}}$  (vol%) and  $\bar{x}_{\text{H}_2,\text{FR}}$  (vol%) are the average O<sub>2</sub> and H<sub>2</sub> concentrations in the air reactor and the fuel reactor, respectively. In the fuel reactor, only H<sub>2</sub> was considered: for the solid fuel-fired CLC, the main reducing gases are H<sub>2</sub> and CO from the devolatilization and gasification, the CH<sub>4</sub> has a low concentration value and can be further converted to H<sub>2</sub> via steam reforming; the reactivity of H<sub>2</sub> and CO mixtures are similar to that of H<sub>2</sub> [32]. The average H<sub>2</sub> concentration ( $\bar{x}_{\text{H}_2,\text{FR}}$ ) is 5 vol% according to Adanez et al.[31,33].

The selected solid fuel is lignite, and its proximate analysis and ultimate analysis results are listed in Table 4. The ilmenite [31], manganese ore [23], and CuO@TiO<sub>2</sub>-Al<sub>2</sub>O<sub>3</sub> [34] oxygen carriers were selected for comparison. The minimum solid inventories for the four oxygen carriers are illustrated in Fig. 11. For CuO@TiO<sub>2</sub>-Al<sub>2</sub>O<sub>3</sub>, the needed solid inventories in the air reactor are 95 kg/MW<sub>th</sub>, which is far higher than the other oxygen carriers, due to the slow oxidization rate. The required solid inventories in the air reactor is only 13 kg/MW<sub>th</sub> for CMTF\_Ind due to the ultrafast oxidization rate. In the fuel reactor, the required minimum bed inventories are 65 kg/MW<sub>th</sub> for CMTF\_Ind, which is far lower than 191 kg/MW<sub>th</sub> for CuO@TiO<sub>2</sub>-Al<sub>2</sub>O<sub>3</sub>, 212 kg/MW<sub>th</sub> for ilmenite, and 274 kg/MW<sub>th</sub> for manganese ore. The total bed inventories are minimum, implying the sizes of the reactors can be reduced a lot. The cost of erecting the CLC unit and oxygen carrier production is promisingly reduced as well.

Table 4. Proximate analysis and ultimate analysis of lignite [35]

Ultimate analysis (wt%)		Proximate analysis (wt%)	
C <sub>ar</sub>	45.4	Mositure <sub>ar</sub>	12.6
H <sub>ar</sub>	2.5	Volatile matter <sub>ar</sub>	28.6
N <sub>ar</sub>	0.6	Fixed carbon <sub>ar</sub>	33.6
S <sub>ar</sub>	5.2	Ash <sub>ar</sub>	25.2

$O_{ar}$	8.5*		
$m_{O_2}$ (kg-O <sub>2</sub> /kg-fuel)	1.2	$H_{fuel}$ (kJ/kg)	16250

\*oxygen to balance

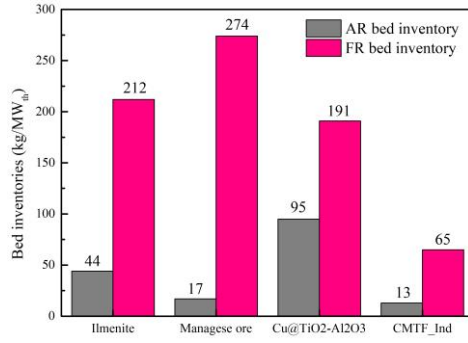


Fig. 11. Required minimum solid inventories for different oxygen carriers (AR: air reactor;  
FR: fuel reactor)

The bed pressure drops in the air reactor ( $\Delta p_{AR}$ , Pa/MW<sub>th</sub>) and the fuel reactor ( $\Delta p_{FR}$ , Pa/MW<sub>th</sub>) are given by

$$\Delta p_{AR} = \frac{m_{OC,AR} g}{A_{AR}} \quad (15)$$

$$\Delta p_{FR} = \frac{m_{OC,FR} g}{A_{FR}} \quad (16)$$

where  $A_{AR}$  (m<sup>2</sup>) and  $A_{FR}$  (m<sup>2</sup>) are the cross sectional areas of the air reactor and the fuel reactor, respectively.

In the actual operation, the energy consumption of fans is a crucial index affecting the CLC power plant efficiency. The fan power should overcome the pressure drops in the air reactor and the fuel reactor. The fan powers for the air reactor ( $\Delta P_{AR,fan}$ , W) and the fuel reactor ( $\Delta P_{FR,fan}$ , W) can be calculated as

$$\Delta P_{AR,fan} = \frac{n}{n-1} \frac{p_{am} \dot{V}_{g,AR}}{\eta_{fan}} \left[ \left( \frac{p_{am} + \Delta p_{bed,AR}}{p_{am}} \right)^{\frac{n-1}{n}} - 1 \right] \quad (17)$$

$$\Delta P_{FR, fan} = \frac{n}{n-1} \frac{p_{am} \dot{V}_{g,FR}}{\eta_{fan}} \left[ \left( \frac{p_{am} + \Delta p_{bed,FR}}{p_{am}} \right)^{\frac{n-1}{n}} - 1 \right] \quad (18)$$

where  $n$  refers to the isentropic coefficient,  $p_{am}$  (Pa) is the fan inlet pressure (assumed to be ambient).  $\dot{V}_{g,AR}$  (m<sup>3</sup>/s) and  $\dot{V}_{g,FR}$  (m<sup>3</sup>/s) are the fan volume flowrates of the air reactor and the fuel reactor at ambient temperature, which are equal to the needed flowrates of fluidizing gases for the reactors.  $\eta_{fan}$  is the fan efficiency.  $\Delta p_{bed,AR}$  (Pa) and  $\Delta p_{bed,FR}$  (Pa) are bed pressure drops of the air reactor and the fuel reactor.

For a 1000 MW<sub>th</sub> CLC designed by Lyngfelt and Leckner [36], The chosen or assumed parameter values are listed in Table 5. The estimated fan powers for the air reactor and the fuel reactor are showed in Fig. 12 for above different oxygen carriers. It can be seen than the total fans power is 989 kW when using the prepared CMTF\_Ind as oxygen carrier, the value is 3.0 to 3.6 times lower than the total fans power when using ilmenite, manganese ore and CuO@TiO<sub>2</sub>-Al<sub>2</sub>O<sub>3</sub>. It will be create a great gain in efficiency for a CLC power plant.

Table 5. Chosen or assumed parameter values

	$A_i$ (m <sup>2</sup> )	$\dot{V}_{g,i}$ (m <sup>3</sup> /s)	$n$	$\eta_{fan}$
AR	198	260	1.4	0.95
FR	77	96	1.4	0.95

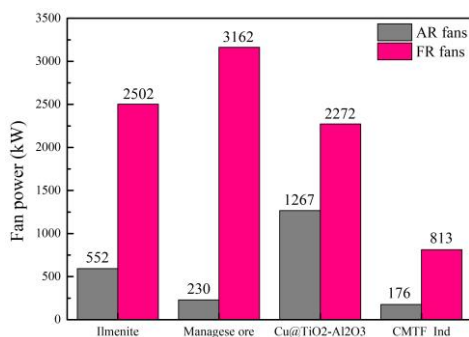


Fig. 12. Esitimated fan energy consumption when using different oxygen carriers (AR: air reactor; FR: fuel reactor)

## Conclusions

The spray drying granulation method was employed to produce the perovskite  $\text{CaMn}_{0.5}\text{Ti}_{0.375}\text{Fe}_{0.125}\text{O}_{3-6}$  particles at an industrial scale (CMTF\_Ind). The fine raw materials are manufactured to CMTF\_Ind particles after the spray drying granulation and the calcination. More than 90% of the prepared CMTF\_Ind particles are in the diameter range of 75-500  $\mu\text{m}$ . The physical and chemical properties were compared with the perovskite prepared at laboratory scale (CMTF\_Lab). Microfluidized bed thermogravimetric analysis (MFB-TGA) experiments were conducted to obtain oxygen uncoupling and redox kinetics of CMTF\_Ind at a wide temperature range. The redox multicycles show that CMTF\_Ind shows no degradation in reactivity and no agglomeration after more than 20 redox cycles. Kinetic experiments, conducted at 900  $^{\circ}\text{C}$ , found that the required time for full oxygen release at the firstly fast stage is  $\sim 20$  s, the full oxidation of CMTF\_Ind can be finished within  $\sim 5$  s, and full reduction with  $\text{H}_2$  can be completed within  $\sim 30$  s. The experimental data of the oxygen uncoupling and redox reactions from the MFB-TGA were well fitted by the simplified two-phase reactor model coupled with a two-stage kinetic model, using the same pre-exponential factors and activation energies as CMTF\_Lab. The comparison of kinetics,

Commented [ZL36]: Lei: this is a bit repeating the first sentence? Skip it?

attrition index and crystalline phase shows CMTF\_Ind shows similar chemical and physical properties as CMTF\_Lab. **Therefore, the upscaling preparation of the perovskite particles at an industrial scale was successfully realized in this work.** Based on the measured kinetics, the required bed inventories are 13 kg/MW<sub>th</sub> in the air reactor and 65 kg/MW<sub>th</sub> in the fuel reactor when using the prepared CMTF\_Ind as the oxygen carrier. Comparing with ilmenite, manganese, CuO@TiO<sub>2</sub>-Al<sub>2</sub>O<sub>3</sub>, the bed inventories are quite low. Moreover, the fan powers to overcome the bed pressures were estimated, and the total fan power is 3.0 to 3.6 times lower than the total fan power when using other oxygen carriers.

## Acknowledgments

Thanks to Mr. Long Chen, Mr. Jinlong He, and Junyi Mao from China Petroleum & Chemical Corporation Research Institute of Petrochemical Industry for supporting the attrition experiments in this work. The research has received funding from the National Natural Science Foundation of China (No. 51976102), the National Key Research and Development Plan of China (No. 2017YFE0112500), and European Union's Horizon 2020 Research and Innovation Program (No. 764697-CHEERS).

## Nomenclature

$A_{0,\text{chem}}$	pre-exponential factor of the fast reaction stage, m <sup>3</sup> /mol/s
$A_{0,\text{diff}}$	pre-exponential factor of the slow reaction stage, m <sup>3</sup> /mol/s
$A_{0,L}$	pre-exponential factor of the critical conversion
$A_i$	cross sectional areas of the air reactor or fuel reactor, m <sup>2</sup>
$Ar$	Archimedes number
$c_{p,\text{OC}}$	specific heat capacity of oxygen carrier, J/kg/K

$C_{b,i}$	concentration of gas $i$ in the bubble phase, mol/m <sup>3</sup>
$C_{e,i}$	concentration of gas $i$ in the emulsion phase, mol/m <sup>3</sup>
$C_{e,i}^*$	equilibrium concentration of gas $i$ , mol/m <sup>3</sup>
$d_p$	diameter of the oxygen carrier particle, m
$D_i$	gas $i$ molecular diffusivity, m <sup>2</sup> /s
$E_{\text{chem}}$	activation energy of the fast reaction stage, kJ/mol
$E_{\text{diff}}$	activation energy of the slow reaction stage, kJ/mol
$E_L$	activation energy of the critical conversion, kJ/mol
$f_a$	volume fraction of oxygen carrier particles in all solid volume
$H_{\text{fuel}}$	low heat value (LHV) of the solid fuel, kJ/kg
$H_{\text{mf}}$	bed height in the bubbling bed reactor, m
$k_{\text{chem}}$	reaction rate constant of the fast reaction stage, m <sup>3</sup> /mol/s
$k_{\text{diff}}$	reaction rate constant of the slow reaction stage, m <sup>3</sup> /mol/s
$k_g$	external mass transfer coefficient, m/s
$K_{\text{be}}$	interchange coefficient between the bubble and emulsion phase, s <sup>-1</sup>
$K_r$	reaction rate constant of particles in the emulsion phase, s <sup>-1</sup>
$K_{\text{ri}}$	reaction rate constant of particles, s <sup>-1</sup>
$m(t)$	mass measured by the weight transducer at time $t$ , g
$m_o$	whole mass of the reactor and oxidized oxygen carrier samples, g
$m_O$	oxygen mass required for full combusting per kg of solid fuel, kg-O <sub>2</sub> /kg-fuel
$m_{\text{OC}}$	mass of the added oxygen carrier samples, g
$m_{\text{OC},i}$	required minimum solid inventories in the air reactor or fuel reactor, kg/MW <sub>th</sub>

$m_r$	whole mass of the reactor and reduced oxygen carrier, g
$M_i$	molar mass of $i$ , kg/mol
$n$	isentropic coefficient
$P_{am}$	fan inlet pressure
$\Delta p_i$	bed pressure drops in the air reactor or fuel reactor, Pa/MW <sub>th</sub>
$\Delta P_{i, fan}$	fan powers of the air reactor or fuel reactor, W
$R_c$	Reynolds number
$R_g$	ideal gases constant, J/mol/K
$R_{OC,ou}$	oxygen transport capacity for oxygen uncoupling, wt.%
$R_{OC,t}$	total oxygen transport capacity, wt.%
$Sh$	Sherwood number
$T$	temperature in Kelvin, K
$U_0$	superficial gas velocity, m/s
$U_b$	bubble rise velocity, m/s
$U_b^*$	effective gas velocity in the bubble phase, m/s
$U_{mf}$	minimum fluidization velocity, m/s
$\dot{V}_{g,i}$	fan volume flowrates of air reactor or fuel reactor at ambient temperature, m <sup>3</sup> /s
$\bar{x}_{j,i}$	average gas $j$ concentration in the air reactor or fuel reactor, vol%
$X$	conversion level of oxidation or reduction reaction at time $t$
$X_{chem}$	conversion level of the fast reaction stage at time $t$
$X_{diff}$	conversion level of the slow reaction stage at time $t$
$X_e$	equilibrium conversion level of an oxygen carrier

$X_o$	conversion level of oxidation reaction at time $t$
$X_{ou}$	conversion level of oxygen uncoupling reaction at time $t$
$X_r$	conversion level of reduction reaction at time $t$
$\alpha$	stoichiometric coefficient
$\rho_s$	particle density of oxygen carrier, kg/m <sup>3</sup>
$\varepsilon_{mf}$	voidage of fluidized bed
$\theta$	fraction of the bubble phase
$\eta_{fan}$	fan efficiency
$\delta$	amount of lattice oxygen
$\gamma$	amount of lattice oxygen
$\psi$	ratio of the conversion level at the fast reaction stage to the conversion level

## References

- [1] J. Adanez, A. Abad, F. Garcia-Labiano, P. Gayan, F. Luis, Progress in chemical-looping combustion and reforming technologies, *Prog. Energ. Combust.* 38(2) (2012) 215-282.
- [2] A. Lyngfelt, Chemical-looping combustion of solid fuels—status of development, *Appl Energy* 113 (2014) 1869-1873.
- [3] T. Mattisson, A. Lyngfelt, H. Leion, Chemical-looping with oxygen uncoupling for combustion of solid fuels, *Int J Greenhouse Gas Control* 3(1) (2009) 11-19.
- [4] T. Mattisson, H. Leion, A. Lyngfelt, Chemical-looping with oxygen uncoupling using CuO/ZrO<sub>2</sub> with petroleum coke, *Fuel* 88(4) (2009) 683-690.
- [5] A. Abad, I. Adánez-Rubio, P. Gayán, F. García-Labiano, F. Luis, J. Adánez, Demonstration of chemical-looping with oxygen uncoupling (CLOU) process in a 1.5 kW<sub>th</sub> continuously operating



- unit using a Cu-based oxygen-carrier, *Int J Greenhouse Gas Control* 6 (2012) 189-200.
- [6] M. Källén, M. Rydén, C. Dueso, T. Mattisson, A. Lyngfelt,  $\text{CaMn}_{0.9}\text{Mg}_{0.1}\text{O}_{3-\delta}$  as Oxygen Carrier in a Gas-Fired 10 kW<sub>th</sub> Chemical-Looping Combustion Unit, *Ind. Eng. Chem. Res.* 52(21) (2013) 6923-6932.
- [7] J. Adánez, P. Gayán, J. Celaya, L. F. de Diego, F. García-Labiano, A. Abad, Chemical looping combustion in a 10 kW<sub>th</sub> prototype using a  $\text{CuO}/\text{Al}_2\text{O}_3$  oxygen carrier: Effect of operating conditions on methane combustion, *Ind Eng Chem Res* 45(17) (2006) 6075-6080.
- [8] Z. Reinking, H. S. Shim, K. J. Whitty, J. S. Lighty, Computational simulation of a 100 kW dual circulating fluidized bed reactor processing coal by chemical looping with oxygen uncoupling, *Int J Greenhouse Gas Control* 90 (2019) 102795.
- [9] C. Linderholm, M. Schmitz, M. Biermann, M. Hanning, A. Lyngfelt, Chemical-looping combustion of solid fuel in a 100 kW unit using sintered manganese ore as oxygen carrier, *Int J Greenhouse Gas Control* 65 (2017) 170-181.
- [10] S. Penthor, F. Zerobin, K. Mayer, T. Pröll, H. Hofbauer, Investigation of the performance of a copper based oxygen carrier for chemical looping combustion in a 120 kW pilot plant for gaseous fuels, *Appl Energy* 145 (2015) 52-59.
- [11] Z. Hamidouche, E. Masi, P. Fede, O. Simonin, K. Mayer, S. Penthor, Unsteady three-dimensional theoretical model and numerical simulation of a 120-kW chemical looping combustion pilot plant, *Chem Eng Sci* 193 (2019) 102-119.
- [12] P. Ohlemüller, M. Reitz, J. Ströhle, B. Epple, Investigation of chemical looping combustion of natural gas at 1 MW<sub>th</sub> scale, *Pro Combust Inst* 37(4) (2019) 4353-4360.
- [13] C. K. Clayton, K. J. Whitty, Measurement and modeling of decomposition kinetics for copper

oxide-based chemical looping with oxygen uncoupling, *Appl. Energy* 116 (2014) 416-423.

[14] W. Hu, F. Donat, S. A. Scott, J. S. Dennis, Kinetics of oxygen uncoupling of a copper based oxygen carrier, *Appl Energy* 161(2016) 92-100.

[15] E. Alonso, C. Hutter, M. Romero, A. Steinfeld, J. Gonzalez-Aguilar, Kinetics of  $Mn_2O_3$ - $Mn_3O_4$  and  $Mn_3O_4$ - $MnO$  Redox reactions performed under concentrated thermal radiative flux, *Energy Fuels* 27 (2013) 4884-4890.

[16] L. Xu, S. Chen, H. Sun, Z. Li, N. Cai, Experimental study of Cu-modified manganese ore for  $O_2$  production in the CLC+ CLOU scheme, *Fuel* 244 (2019) 69-75.

[17] M. M. Hossain, H. I. e Lasa, Reactivity and stability of Co - Ni/ $Al_2O_3$  oxygen carrier in multicycle CLC, *AIChE journal* 53(7) (2007) 1817-1829.

[18] E.I. Leonidova, I.A. Leonidov, M.V. Patrakeev, V.L. Kozhevnikov, Oxygen non-stoichiometry, high-temperature properties, and phase diagram of  $CaMnO_{3-\delta}$ , *J. Solid State Electrochem.* 15 (2011) 1071-1075.

[19] L. F. de Diego, A. Abad, A. Cabello, P. Gayán, F. García-Labiano, J. Adánez, Reduction and oxidation kinetics of a  $CaMn_{0.9}Mg_{0.1}O_{3-\delta}$  oxygen carrier for chemical-looping combustion, *Ind. Eng. Chem. Res.* 53(1) (2013) 87-103.

[20] W. Xing, M. L. Fontaine, Z. Li, J. MPolfus, Y. Larring, CDenonville, R. Bredesen, Asymmetric tubular  $CaTi_{0.6}Fe_{0.15}Mn_{0.25}O_{3-\delta}$  membranes: Membrane architecture and long-term stability, *J. Membrane Sci.* 548 (2018) 372-379.

[21] H. Leion, Y. Larring, E. Bakken, R. Bredesen, T. Mattisson, A. Lyngfelt, Use of  $CaMn_{0.875}Ti_{0.125}O_3$  as Oxygen Carrier in Chemical Looping with Oxygen Uncoupling, *Energy Fuels* 23 (2009) 5276-5283.

- [22] L. Liu, Z. Li, Z. Li, Y. Larring, N. Cai, Heterogeneous reaction kinetics of a perovskite oxygen carrier for chemical looping combustion coupled with oxygen uncoupling, *Chem Eng J* 417 (2021) 128054.
- [23] Y. Li, Z. Li, L. Liu, N. Cai, Measuring the fast oxidation kinetics of a manganese oxygen carrier using microfluidized bed thermogravimetric analysis, *Chem. Eng. J.* 385 (2020) 123970.
- [24] A. Abad, A. Cabello, P. Gayán, F. García-Labiano, L. F. de Diego, T. Mendiara, J. Adánez, Kinetics of  $\text{CaMn}_{0.775}\text{Ti}_{0.125}\text{Mg}_{0.1}\text{O}_{2.9-8}$  perovskite prepared at industrial scale and its implication on the performance of chemical looping combustion of methane, *Chem. Eng. J.* (2020) 124863. Accepted.
- [25] Y. Li, H. Wang, W. Li, Z. Li, N. Cai,  $\text{CO}_2$  Gasification of a Lignite Char in Microfluidized Bed Thermogravimetric Analysis for Chemical Looping Combustion and Chemical Looping with Oxygen Uncoupling, *Energy fuels* 33(1) (2018) 449-459.
- [26] Y. Li, Z. Li, H. Wang, N. Cai, CaO carbonation kinetics determined using micro-fluidized bed thermogravimetric analysis, *Fuel* 264 (2020) 116823.
- [27] D. Kunii, O. Levenspiel, *Fluidization Engineering*, Butterworth-Heinemann, Newton, U.S.A. ,1991, p. 155.
- [28] ASTM, D5757-95: Standard Test Method for Determination of Attrition and Abrasion of Powdered Catalysts by Air Jets, ASTM, Philadelphia (1995).
- [29] A. Cabello, P. Gayán, F. García-Labiano, L. F. De Diego, A. Abad, J. Adánez, On the attrition evaluation of oxygen carriers in Chemical Looping Combustion, *Fuel Pro Tech* 148(2016) 188-197.
- [30] L. Liu, Z. Li, L. Wang, Z. Zhao, Y. Li, N. Cai, MgO–Kaolin-supported manganese ores as oxygen carriers for chemical looping combustion, *Ind. Eng. Chem. Res.* 59(15) (2019) 7238-7246.

- [31] A. Abad, J. Adanez, A. Cuadrat, F. Garcia-Labiano, P. Gayan, F. Luis, Kinetics of redox reactions of ilmenite for chemical-looping combustion, *Chem. Eng. Sci.* 66(4) (2011) 689-702.
- [32] A. Abad, F. Garcia-Labiano, L. F. de Diego, P. Gayán, J. Adánez, Reduction kinetics of Cu-, Ni-, and Fe-based oxygen carriers using syngas (CO+ H<sub>2</sub>) for chemical-looping combustion, *Energy Fuels* 21(4) (2007) 1843-1853.
- [33] J. Adánez, A. Cuadrat, A. Abad, P. Gayán, L. F. de Diego, F. Garcia-Labiano, Ilmenite activation during consecutive redox cycles in chemical-looping combustion, *Energy Fuels* 24(2) (2010) 1402-1413.
- [34] X. Tian, M. Su, H. Zhao, Kinetics of redox reactions of CuO@TiO<sub>2</sub>-Al<sub>2</sub>O<sub>3</sub> for chemical looping combustion and chemical looping with oxygen uncoupling, *Combust. Flame* 213 (2020) 255-267.
- [35] I. Adánez-Rubio, P. Gayán, A. Abad, F. García-Labiano, L. F. De Diego, J. Adánez, Kinetic analysis of a Cu-based oxygen carrier: Relevance of temperature and oxygen partial pressure on reduction and oxidation reactions rates in Chemical Looping with Oxygen Uncoupling (CLOU), *Chem. Eng. J.* 256(2014) 69-84.
- [36] A. Lyngfelt, B. Leckner, A 1000 MWth boiler for chemical-looping combustion of solid fuels- Discussion of design and costs, *Appl. Energy* 157 (2015) 475-487.